8-31-2022

Excitation-Dependent Photoluminescence of BaZrO3:Eu3+ Crystals

Santosh K. Gupta

Hisham Abdou
The University of Texas Rio Grande Valley

Carlo U. Segre

Yuanbing Mao

Recommended Citation

Gupta, S.K.; Abdou, H.; Segre, C.U.; Mao, Y. Excitation-Dependent Photoluminescence of BaZrO3:Eu3+ Crystals. Nanomaterials 2022, 12, 3028. https://doi.org/10.3390/nano12173028

nanomaterials

MDPI

Article

Excitation-Dependent Photoluminescence of $BaZrO_3$:Eu^{3+} Crystals

Santosh K. Gupta [1,2], Hisham Abdou [3], Carlo U. Segre [4] and Yuanbing Mao [5,*]

[1] Radiochemistry Division, Bhabha Atomic Research Centre, Trombay, Mumbai 400085, India
[2] Homi Bhabha National Institute, Anushakti Nagar, Mumbai 400094, India
[3] Department of Chemistry, University of Texas Rio Grande Valley, 1201 West University Drive, Edinburg, TX 78539, USA
[4] Center for Synchrotron Radiation Research and Instrumentation and Department of Physics, Illinois Institute of Technology, Chicago, IL 60616, USA
[5] Department of Chemistry, Illinois Institute of Technology, 3105 South Dearborn Street, Chicago, IL 60616, USA
* Correspondence: ymao17@iit.edu; Tel.: +1-312-567-3815

Abstract: The elucidation of local structure, excitation-dependent spectroscopy, and defect engineering in lanthanide ion-doped phosphors was a focal point of research. In this work, we have studied Eu^{3+}-doped $BaZrO_3$ (BZOE) submicron crystals that were synthesized by a molten salt method. The BZOE crystals show orange–red emission tunability under the host and dopant excitations at 279 nm and 395 nm, respectively, and the difference is determined in terms of the asymmetry ratio, Stark splitting, and intensity of the uncommon $^5D_0 \rightarrow {}^7F_0$ transition. These distinct spectral features remain unaltered under different excitations for the BZOE crystals with Eu^{3+} concentrations of 0–10.0%. The 2.0% Eu^{3+}-doped BZOE crystals display the best optical performance in terms of excitation/emission intensity, lifetime, and quantum yield. The X-ray absorption near the edge structure spectral data suggest europium, barium, and zirconium ions to be stabilized in +3, +2, and +4 oxidation states, respectively. The extended X-ray absorption fine structure spectral analysis confirms that, below 2.0% doping, the Eu^{3+} ions occupy the six-coordinated Zr^{4+} sites. This work gives complete information about the BZOE phosphor in terms of the dopant oxidation state, the local structure, the excitation-dependent photoluminescence (PL), the concentration-dependent PL, and the origin of PL. Such a complete photophysical analysis opens up a new pathway in perovskite research in the area of phosphors and scintillators with tunable properties.

Keywords: $BaZrO_3$; europium; luminescence; EXAFS; defect

Citation: Gupta, S.K.; Abdou, H.; Segre, C.U.; Mao, Y. Excitation-Dependent Photoluminescence of $BaZrO_3$:Eu^{3+} Crystals. *Nanomaterials* **2022**, *12*, 3028. https://doi.org/10.3390/nano12173028

Academic Editor: Wojciech Pisarski

Received: 24 July 2022
Accepted: 25 August 2022
Published: 31 August 2022

1. Introduction

The trivalent europium ion Eu^{3+} is considered to be one of the most sensitive lanthanide ions that displays environment- and symmetry-sensitive emissions owing to its pure magnetic dipole transition (MDT, $\Delta J = \pm 1$), hypersensitive electric dipole transition (HEDT, $\Delta J = \pm 2$), and neither magnetic nor electric $^5D_0 \rightarrow {}^7F_0$ ($\Delta J = 0$) transition [1–4]. When Eu^{3+} is localized at a highly symmetric site with a center of inversion (C_i), its MDT predominates over its EDT. If Eu^{3+} is situated at a highly asymmetric site, its emission is the other way around [5]. In addition, the Eu^{3+} ion is one of the most fascinating dopant ions for quality red phosphors with a high quantum yield (QY), a decent thermal stability, and a long luminescence lifetime [6,7].

Perovskites with a generic formula ABO_3 are in high demand as luminescence hosts due to their structural flexibility, wide band gap, ease of doping, and ability to accommodate lanthanide ions at both A and B sites [8–10]. Among them, $BaZrO_3$ (BZO) is a unique material due to its wide tunable band gap (5.6 eV) [11], high refractive index [12], high proton conductivity, and high chemical and mechanical stability [10,13–15]. It has various applications in the areas of luminescence [16], catalysis [16,17], proton-conducting solid oxide fuel cells [18,19], and many others. Eu^{3+} ion-doped ABO_3 perovskites have attracted a

lot of attention due to their high thermal and chemical stability, low environmental toxicity, and various applications in photocatalysis, white light generation [20], light emitting diodes (LEDs) [21], and bioimaging [22].

One can probe the local sites of Eu^{3+} ions in ABO_3 perovskites based on the ratio, spectral splitting, and appearance of $^5D_0 \rightarrow {}^7F_J$ (J = 0–4) emissions.[1] This kind of study is crucial to make materials with optimum light emitting properties. For example, Kunti et al. recently observed MDT and HEDT emissions with $I_{MDT} >>> I_{HEDT}$ along with the host emission under the 275 nm excitation from their $BaZrO_3$:Eu samples synthesized by the solid state route [23]. There was a systematic host-to-dopant energy transfer with an increasing Eu^{3+} doping concentration. Based on the analysis of extended X-ray absorption fine structure (EXAFS) spectroscopic data, they concluded that Eu^{3+} ions were localized at Zr^{4+} sites [23]. Gupta, one of the co-authors of the current manuscript, and his coworkers observed spectral profiles with $I_{HEDT} >>> I_{MDT}$ under various excitations from gel combustion-synthesized BZO:Eu samples [12], which was exactly opposite to what was observed by Kunti et al. [23]. Gupta et al. also proposed that a large fraction of Eu^{3+} ions occupied Zr^{4+} sites based on population analysis of lifetime spectra [12]. Kanie et al. synthesized BZO samples with different sizes and shapes and investigated their effects on luminescence [24].

There were also reports on Eu^{3+}-doped perovskites of $SrZrO_3$, $SrSnO_3$, $BaTiO_3$, $BaSnO_3$, and $BaZr_xTi_{1-x}O_3$. For example, Basu et al. proposed that Eu^{3+} ions resided at Sr^{2+} sites at low dopant concentrations and were distributed at both Sr^{2+} and Sn^{4+} sites at high doping levels in their polyol-synthesized $SrSnO_3$ nanoparticles based on EXAFS measurements [25]. The same group further proposed that Eu^{3+} ions occupied the centrosymmetric Sr^{2+} sites up to 1.5% Eu^{3+} doping and, beyond that, the synthesized $SrSnO_3$ nanoparticles formed a separate europium oxide phase based on time resolved emission spectroscopy (TRES) and electron paramagnetic resonance (EPR) studies. Similarly, based on EXAFS studies, Rabufetti et al. found that Eu^{3+} ions resided at Ba^{2+} sites at low dopant concentrations (up to 4% Eu^{3+} doping) but were distributed at both Ba^{2+} and Ti^{4+} sites at high doping levels in their vapor-diffusion sol-gel-synthesized $BaTiO_3$ nanocrystals [26]. Canu et al. have tuned the photoluminescence properties of Eu^{3+}-doped $BaZr_xTi_{1-x}O_3$ perovskite by applying an electric field [27].

There are also reports that studied the effect of changing the A cation of $AZrO_3$:Eu on the luminescence emission intensities [28]. Katyayan et al. studied the impact of co-doping Tb^{3+} with Eu^{3+} on the optical and spectroscopic characteristics of BZO perovskite [29]. Another study investigated the effect of particle size and morphology on the fluorescence behaviors of these metal oxides [24].

Color tunability is achieved from samples with the same dopants and hosts by simply varying the excitation wavelength. For example, Gupta et al. showed different emission characteristics of $SrZrO_3$:Eu^{3+} nanoparticles in terms of the asymmetry ratio (A_{21}) under the excitations with host absorption, charge transfer, and the *f-f* band of Eu^{3+} [30]. Guo et al. synthesized a Bi^{3+} and Eu^{3+} ion co-doped $Ba_9Lu_2Si_6O_{24}$ single-phased phosphor via a conventional high-temperature solid-state reaction [31]. They demonstrated that the relative emission intensity of Bi^{3+} luminescent centers tightly depends on the incident excitation wavelength due to the complex energy transfer processes among these Bi^{3+} centers.

Furthermore, even though the induced electric dipole (ED) $^5D_0 \rightarrow {}^7F_0$ transition is strictly forbidden by the ΔJ selection rule of the Judd–Ofelt theory, there are reported occurrences of it as a well-known example of the breakdown of the selection rules of the Judd–Ofelt theory [1]. For example, Guzmán-Olguín et al. showed an unusual great intensity of the $^5D_0 \rightarrow {}^7F_0$ transition centered at 580 nm when they excited their Eu^{3+}-doped $BaHfO_3$ perovskite ceramic under UV radiation with the wavelength associated with the charge transfer band (272 nm), while this transition was very weak when the sample was excited at 396 or 466 nm wavelengths [32]. One of the co-authors of this manuscript, Gupta, with his co-workers, reported the presence of two Stark components in the $^5D_0 \rightarrow {}^7F_0$ transition from their $Nd_2Zr_2O_7$:Eu phosphor when excited at 256 nm [33].

It is clear that there is no systematic investigation of the luminescence of BZO:Eu nor studies on its $^5D_0 \rightarrow {}^7F_0$ transition under host and Eu^{3+} excitations. In this work, we have first synthesized BZO:Eu submicron crystals using an environmentally friendly molten salt synthesis (MSS) method based on the report by Zhou et al. using barium oxalate and zirconium oxide as precursors and a KOH/NaOH salt mixture as the reaction medium [34]. We studied tuning the red to orange emission ratio from the BZO:Eu crystals by modulating the excitation wavelength and deciphered the local site occupancy of Eu^{3+} ions in BZO with Eu, Ba, and Zr-edge EXAFS analysis. More importantly, other than the weak $^5D_0 \rightarrow {}^7F_3$ at 653 nm, we observed a strong $^5D_0 \rightarrow {}^7F_0$ transition, which is known to be strictly forbidden by both EDT and MDT of Eu^{3+} ions, as based on the Judd–Ofelt theory. This observation suggests the deviation of luminescence properties of the Eu^{3+} dopant in the BZO host from the Judd–Ofelt theory. In other words, it indicates that Eu^{3+} ions are localized in highly asymmetric environments, e.g., C_n, C_{nv}, and C_s point group symmetry, so that the selection rules are relaxed to some extent by the mixing of a low-energy charge transfer state with the $4f^6$ configuration [1]. Moreover, designing functional materials that display excitation wavelength-dependent color tunability and understanding structure–property correlation is invaluable to materials scientists.

2. Experimental

The synthesis and instrumentation characterization of the BZO and BZOE submicron crystals are described in detail in the electronic supplementary information as S1. Briefly, six $Ba_{1-x}ZrO_3$:x%Eu^{3+} (x = 0, 0.5, 1.0, 2.0, 5.0, 10.0) samples were synthesized using the MSS method following a procedure published previously with one of the co-authors of this manuscript. Based on the Eu^{3+} doping levels, the synthesized $Ba_{1-x}ZrO_3$:x%Eu^{3+} samples with x = 0, 0.5, 1.0, 2.0, 5.0, 10.0 are designated as BZO, BZOE-0.5, BZOE-1, BZOE-2, BZOE-5, and BZOE-10, respectively.

3. Results and Discussion

3.1. XRD Patterns

The XRD patterns of the BZO and BZO:Eu samples (Figure 1a) demonstrated that the diffraction peaks of all samples match with the cubic perovskite phase (*Pm*-3*m*) of BZO (JCPDS No. 74-1299) and no impurity peaks were observed. The substitution of Eu^{3+} for constituent ions is evidently aliovalent and may generate oxygen vacancies when resided at a Zr^{4+} site. In case if some fraction resides at a Ba^{2+} site, the charge compensation may invoke the creation of barium vacancies. As seen in Table 1, the cell parameter variation is complex, which means different defect complex generations at different doping levels.

Table 1. Lattice constants and crystallite sizes of the BZOE obtained from Rietveld refinement of the XRD data shown in Figure 1a.

%Eu	0.0	0.5	1.0	2.0	5.0	10.0
a (Å)	4.1947 (2)	4.1954 (3)	4.1944 (3)	4.1952 (3)	4.1976 (3)	4.1971 (2)
Size (nm)	156 (5)	127 (4)	111 (3)	127 (3)	102 (2)	162 (5)

3.2. FTIR and Raman Spectroscopy

To further confirm the formation of the perovskite phase and rule out the formation of other phases, FTIR spectra of the samples were collected (Figure 1b). The only observed peak around 570 cm^{-1} can be assigned to the anti-symmetric stretching Zr–O bond of the octahedral ZrO_6 unit of the $BaZrO_3$ lattice [35–37].

In the Raman spectra of the BZO and BZOE samples (Figure 1c), the peak around 600–900 cm^{-1} is attributed to the symmetric stretch (ν) of the Zr–O bonds in $BaZrO_3$ [23]. With an increasing Eu^{3+} doping level, two extra peaks around 283 and 338 cm^{-1} that correspond to symmetric A_g and degenerated F_g modes of the stretching vibrations of the C_2-octahedron (Eu_2-O) started to appear [38]. This means that Eu^{3+} ions stop going into

the BZO lattice and precipitate as a separate phase of Eu_2O_3 at the doping concentration of 10.0%, which is similar to what Basu et al. observed from their polyol-synthesized $SrSnO_3$ nanoparticles based on EXAFS measurements [25]. The peaks between 100 and 230 cm^{-1} can be assigned to $BaCO_3$ impurity, which did not show up in the XRD patterns and FTIR spectra due to a low percentage. The carbonate phase probably resulted from the chemisorption of atmospheric CO_2 on the surface of the BZO crystals upon its exposure to air. It was reported that the existence of such an impurity phase has no effect on the luminescence properties of the BZO perovskite [8].

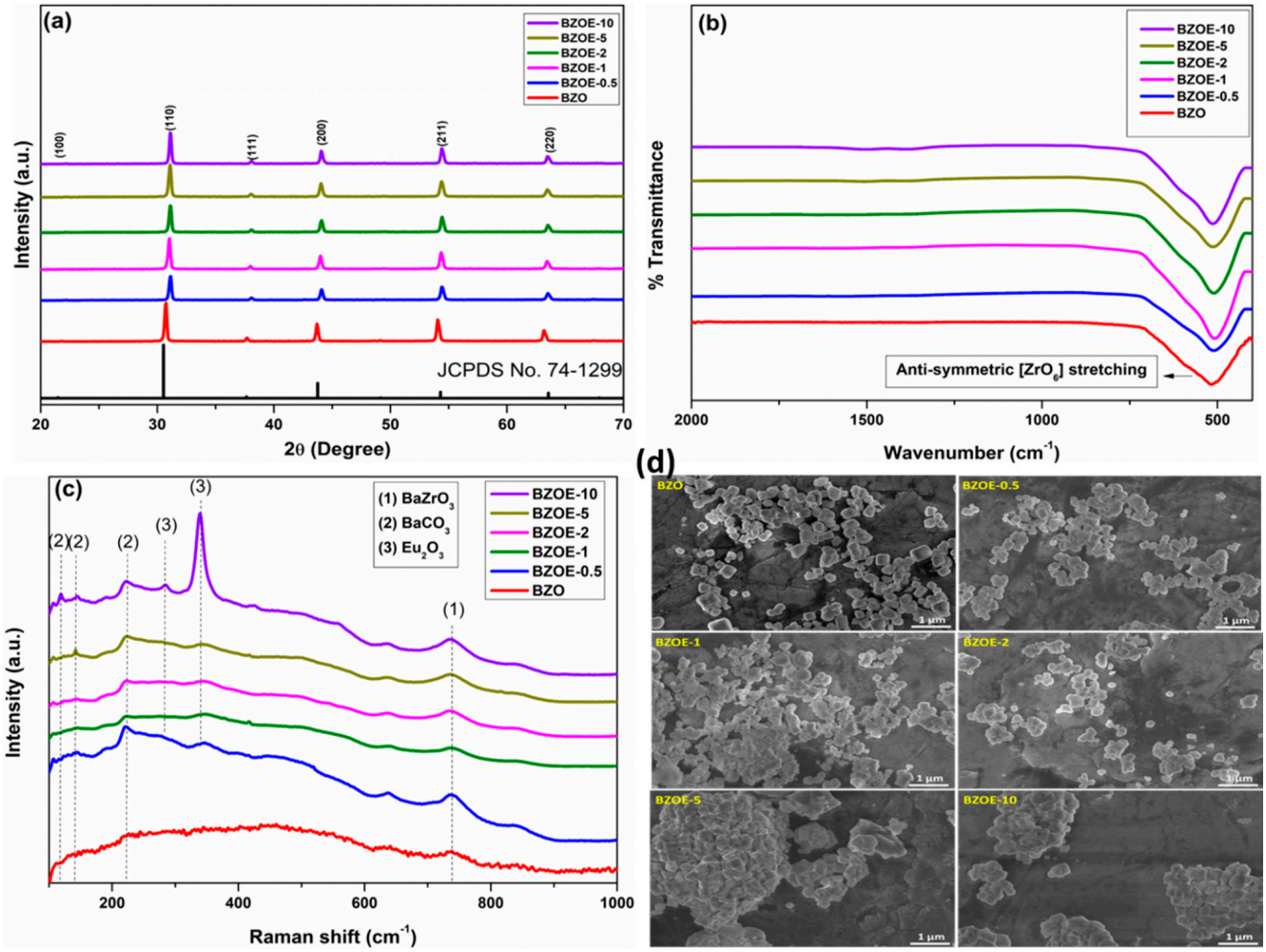

Figure 1. (**a**) XRD patterns, (**b**) FTIR spectra, (**c**) Raman spectra, and (**d**) SEM images of the BZO and BZOE samples.

3.3. SEM Images

The SEM images of the BZO and BZOE samples (Figure 1d) demonstrated that the particles were composed of a mixture of spheres and cubes with well-defined edges. In our earlier work, we found that cubic BZO microcrystals predominated when the synthesis was conducted at a higher annealing temperature. There was almost an equal number of spherical and cubical particles from these samples. No difference in the shape of the particles was noticed from these samples with different Eu^{3+} doping concentrations. However, the agglomeration of the particles increased with an increasing Eu^{3+} concentration. Based on the particle size distribution histograms of these samples obtained using the ImageJ software (Figure S1) and the crystallite sizes obtained from the XRD data (Table 1, Figure S2), no clear correlation between the average particle size and the Eu^{3+} doping concentration was established.

3.4. X-ray Absorption Spectroscopy

3.4.1. XANES

Figure 2a–c shows the normalized XANES spectra of three BZOE samples along with their standards (either the undoped BZO crystals or commercial Eu_2O_3 powder) at the Ba L_3 (Figure 2a), Zr K (Figure 2b), and Eu L_3 (Figure 2c) edges, respectively. The normalized XANES spectra at the Ba L_3-edge shown in Figure 2a are characterized by a sharp white line, which is the main absorption peak due to the transition $2p_{3/2} \rightarrow 5d$. There is no appreciable difference in this edge upon Eu^{3+} doping.

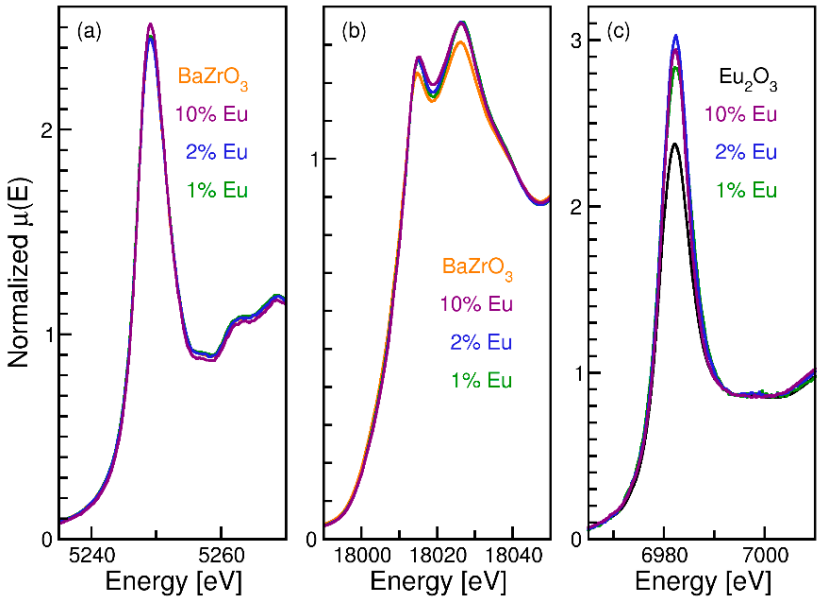

Figure 2. Normalized XANES spectra of the BZOE samples and standards at the (**a**) Ba L_3-edge, (**b**) Zr K-edge, and (**c**) Eu L_3-edge.

It can be seen from Figure 2b that the Zr absorption edges of the BZOE samples coincide with that of the BZO sample, confirming that the oxidation state of Zr is 4+ in the doped samples. Two peaks, A (18,010 eV) and B (18,021 eV), observed in the BZO and BZOE samples just above the Zr absorption edge, are similar to those obtained by Fassbender et al. [39] and Giannici et al. [40] and are due to the octahedral oxygen coordination of Zr^{4+} in the samples. The overall shape of the Zr XANES spectra remains nearly unchanged upon Eu^{3+} doping, and it is suggested that the octahedral symmetry of the Zr atom does not break with doping. The slight increase in the A and B peaks of the doped samples compared to BZO suggest that the Eu^{3+} solubility is very limited (no more than 1–2%).

The Eu L_3-edge XANES spectra of the samples (Figure 2c) show that the absorption edges coincide with that of the standard Eu_2O_3 sample, suggesting that the Eu dopant remains in the Eu^{3+} oxidation state in the BZOE samples. The increase in the white line at the edge indicates an increase in the empty Eu d-states at the Fermi level in the BZOE samples compared to Eu_2O_3, suggesting that the Eu^{3+} is at least partially in a different local environment than in Eu_2O_3.

3.4.2. EXAFS

Figure 3 presents the k^2-weighted Fourier transformed spectra, $|\chi(R)|$, of the BZO and BZOE samples (and Eu_2O_3 standard) at the Ba L_3 (Figure 3a), Zr K (Figure 3b), and Eu L_3 (Figure 3c) edges. For BZO in a cubic perovskite structure (ABO_3) with the space group *Pm*-3*m*, the Zr atoms are coordinated with 6 O atoms in a regular octahedral (6-fold (ZrO_6)) shape and the Ba atoms are coordinated with 12 O atoms in a cuboctahedral (12-fold (BaO_{12})) shape in the first coordination shells. Theoretical EXAFS spectra have

been generated using the above structure for the Ba (Figure S3), Zr (Figure S4), and Eu (Figure S5) edges of the BZO and BZOE samples and fitted to the experimental data.

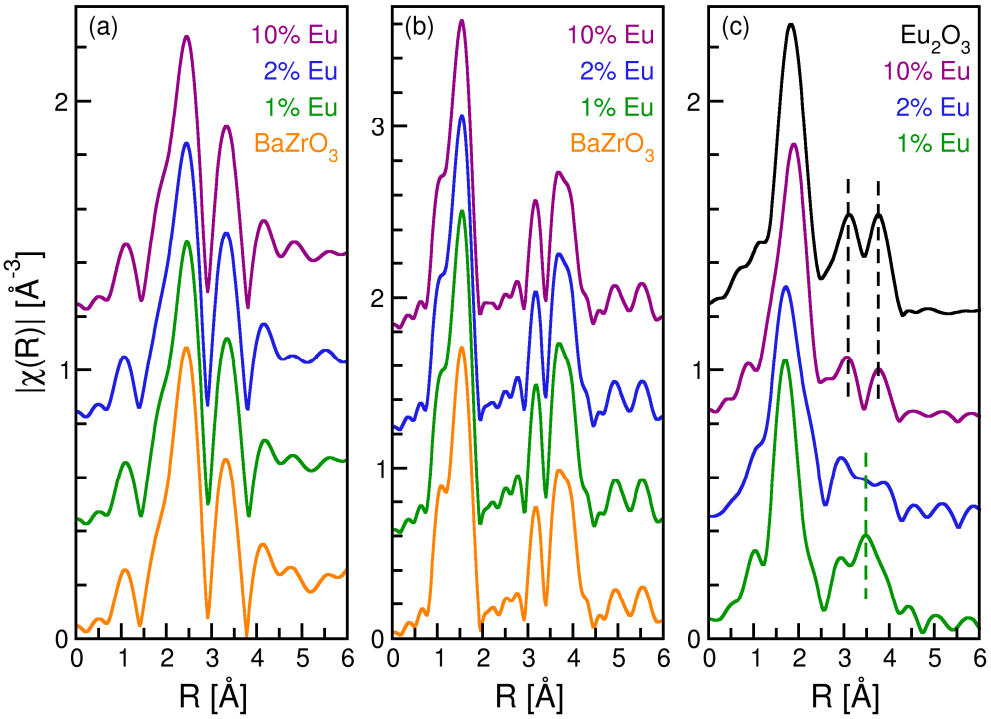

Figure 3. Fourier transformed spectra of the BZOE samples and standards at the (**a**) Ba L_3 edge, (**b**) Zr K edge, and (**c**) Eu L_3 edge. Spectra are shifted vertically for clarity.

Specifically, the Ba edge was fitted with a structural model including three paths, Ba–O (12-fold), Ba–Zr (8-fold), and Ba–Ba (6-fold). For the Ba edge fits, the path degeneracies were held constant and the σ^2 of the Ba–Zr and Ba–Ba paths were constrained to be identical. Windows of 2.0 Å^{-1} < k < 8.5 Å^{-1} with dk = 2.0 and 1.5 Å < R < 3.7 Å with dR = 0.2 were used for the Fourier transformation and fits, respectively. The fit results for the Ba–O paths of each sample are presented in Table 2 and they indicate that the Ba environment is unchanged by Eu doping. The results for the other paths are in Table S1.

Table 2. Values of the amplitude reduction factor (S_0^2) or path degeneracy (N), bond length, and disorder factor for the near neighbor paths obtained from EXAFS analysis of the BZO and BZOE samples at the Ba L_3, Zr K, and Eu L_3 edges.

Scattering Path	Parameter	BZO	BZOE-1	BZOE-2	BZOE-10
Ba–O N = 12	S_0^2	0.74 ± 0.16	0.78 ± 0.18	0.80 ± 0.17	0.78 ± 0.17
	R (Å)	2.91 ± 0.02	2.91 ± 0.02	2.91 ± 0.02	2.91 ± 0.02
	σ^2	0.011 ± 0.005	0.013 ± 0.005	0.013 ± 0.005	0.013 ± 0.005
Zr–O N = 6	S_0^2	0.90 ± 0.10	1.0 ± 0.1	1.0 ± 0.1	1.1 ± 0.1
	R (Å)	2.10 ± 0.01	2.10 ± 0.01	2.10 ± 0.01	2.11 ± 0.01
	σ^2	0.004 ± 0.001	0.005 ± 0.002	0.005 ± 0.002	0.006 ± 0.002
Scattering Path	**Parameter**	**Eu_2O_3**	**BZOE-1**	**BZOE-2**	**BZOE-10**
Eu–O S_0^2 = 0.86	N	7	6.7 ± 1.7	9.8 ± 1.9	7.9 ± 0.7
	R (Å)	2.35 ± 0.01	2.27 ± 0.03	2.33 ± 0.02	2.39 ± 0.01
	σ^2	0.012 ± 0.002	0.012 ± 0.002	0.012 ± 0.002	0.012 ± 0.002

The Zr edges were modeled out to 4 Å using three single scattering paths, Zr–O (6-fold), Zr–Ba (8-fold), and Zr–Zr (6-fold), plus the three high amplitude linear multiple scattering paths. The path degeneracies were held constant for all paths and all the multiple scattering paths are constrained to have the same ΔR as the Zr–Zr path and a common σ^2 parameter. Windows of 2.0 $Å^{-1} < k < 13.0$ $Å^{-1}$ with dk = 2.0 and 1.0 Å < R < 4.3 Å with dR = 0.2 were used for the Fourier transformation and fits, respectively. Table 2 reports the fit results for the Zr–O single scattering path with the other paths reported in Table S2. For all samples, the Ba–Zr and Zr–Ba paths are distances and disorder parameters and are consistent as are the Ba–Ba and Zr–Zr paths. The quality of the Zr edge fits (Figure S4) are limited by the constraints applied but are consistent across all samples, suggesting only limited Eu^{3+} doping at the Zr site.

The Eu L_3 EXAFS presented in Figure 3c clearly show that the 10.0% doped sample exhibits two peaks at ~3.1 Å and ~3.7 Å, which are characteristic of Eu_2O_3. As the doping level is reduced, these two peaks vanish to be replaced by two small peaks at ~3.0 Å and ~3.5 Å, similar to those observed in the Zr edge EXAFS. The Eu edges were modeled only to the first shell, as the attempts to model the longer paths were unsuccessful. The amplitude reduction factor $S_0{}^2$ was held constant at the value determined by fitting the Eu_2O_3 data. The path length, degeneracy, and disorder of the single Eu–O path being modeled were allowed to vary. Windows of 2.0 $Å^{-1} < k < 9.0$ $Å^{-1}$ with dk = 2.0 and 1.0 Å < R < 2.4 Å with dR = 0.2 were used for the Fourier transformation and fits, respectively (Figure S5). The resulting fit parameters are reported in Table 2 and it is clear that the Eu–O distance and the path degeneracy increase with the doping level. At 1.0% doping, the Eu–O distance is 2.25 Å, which is longer than the Zr–O distance but significantly shorter than both the Ba–O and the Eu–O distances in Eu_2O_3. As the doping level increases, the Eu-O distance increases and then exceeds that found in Eu_2O_3. Similarly, the path degeneracy for the 1.0% sample is close to six, as would be expected for doping on the Zr site and increases to a value greater than that in Eu_2O_3. These results strongly suggest that Eu^{3+} at low doping levels sits at the Zr site and has a solubility limit between 1.0–2.0%. At higher concentrations, Eu^{3+} ions are found in a Eu_2O_3-like local environment. This result is consistent with the change in the white line of the Eu XANES, which increases for 1.0% and 2.0% but decreases for 10%.

3.5. PL Spectra

The concentration-dependent excitation spectra (λ_{em} = 625 nm, Figure 4a) and emission spectra (λ_{ex} = 279 nm and 395 nm, Figure 4b,c) of the BZOE samples demonstrated characteristic PL features of the Eu^{3+} dopant in solid-state hosts [41,42]. In general, there is no change of the excitation and emission spectral profiles, Stark splitting, and relative intensity of excitation and emission peaks under the same excitation wavelength among the BZOE samples with the tested Eu^{3+} doping concentrations. The spectra also clearly show that the 2.0% Eu^{3+}-doped sample, BZOE-2, has the highest emission intensity among our samples using the MDT $^5D_0 \rightarrow {}^7F_1$ as an example (Figure 4d).

The excitation spectra of the BZOE samples with λ_{em} = 625 nm corresponding to the $^5D_0 \rightarrow {}^7F_2$ transition of Eu^{3+} ions consisted of two main features (Figure 4a): a broad band extending from 240–320 nm and several fine peaks in the range of 350–500 nm. The broad band peaking around 279 nm is attributed to the allowed charge transfer band (CTB) of electrons from the filled 2p orbital of O^{2-} to the vacant 4d-orbital of the Eu^{3+} ion. The fine peaks around 361, 375, 383, 387, 395, 405, 414, 456, 465, and 472 nm are attributed to the intra f-f transitions of Eu^{3+} ions. The main peaks located at 395 nm and 465 nm are attributed to $^7F_0 \rightarrow {}^5L_6$ and $^7F_0 \rightarrow {}^5D_2$, respectively.

Under the excitations of λ_{ex} = 279 and 395 nm, the emission spectra of the BZOE samples displayed the CTB and several fine peaks corresponding to $^5D_0 \rightarrow {}^7F_J$ (J = 0–4) transitions of Eu^{3+} in the spectral range of 550–750 nm (Figure 4b). Interestingly, several significant differences in terms of the appearance of $^5D_0 \rightarrow {}^7F_0$ transition, the asymmetry

ratio (A_{21}), and Stark splitting were observed from the emission spectra of the BZOE samples in the spectral range of 550–750 nm under these two excitation wavelengths.

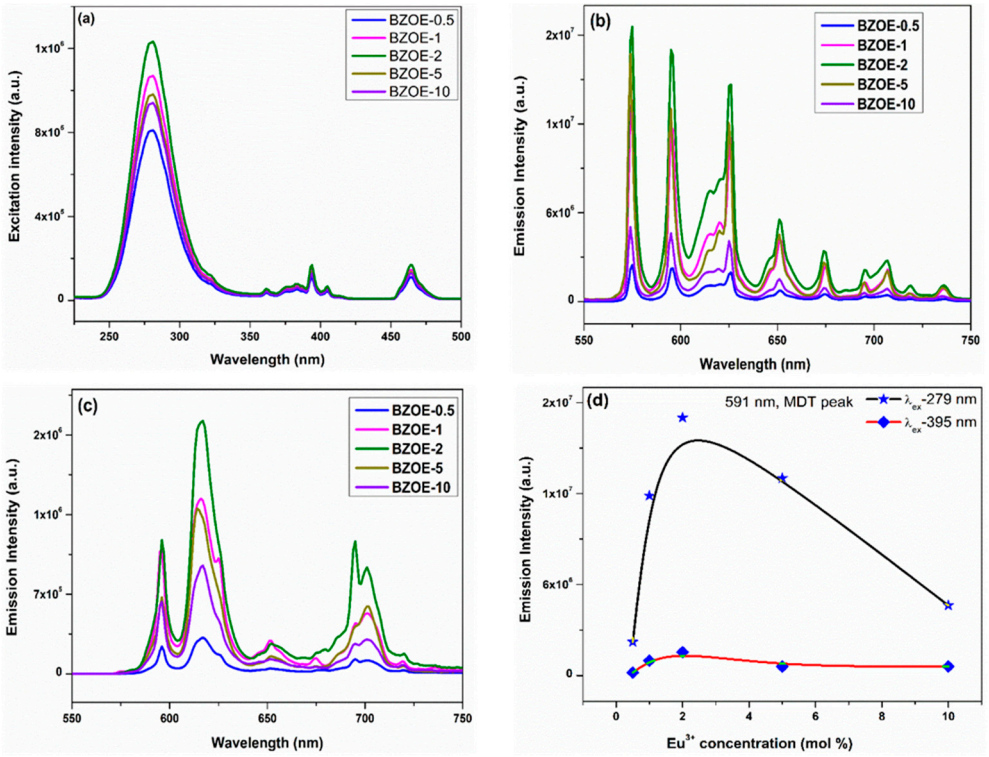

Figure 4. (**a**) Excitation spectra with λ_{em} = 625 nm, emission spectra under (**b**) λ_{ex} = 279 nm and (**c**) λ_{ex} = 395 nm of the BZOE samples. (**d**) Effects of Eu^{3+} doping concentration of the BZOE samples on integrated MDT emission intensity of $^5D_0 \rightarrow {}^7F_1$ transition.

Figure 5a shows a close look of the emission spectra using the BZOE-2 sample as an example. Specifically, under the 395 nm excitation, intense emission bands at 591 nm ($^5D_0 \rightarrow {}^7F_1$, MDT), 612 nm ($^5D_0 \rightarrow F_2$, HEDT), 701 nm ($^5D_0 \rightarrow {}^7F_4$), and 653 nm ($^5D_0 \rightarrow {}^7F_3$, weak peak) were observed [43]. There is no signature of $^5D_0 \rightarrow {}^7F_0$ transition. The integral intensity of the HEDT at 612 nm is stronger than that of the MDT at 591 nm. The $^5D_0 \rightarrow {}^7F_3$ transition is known to be allowed by neither MDT nor EDT. It is forbidden in nature according to the Judd–Ofelt (J–O) theory but could gain intensity via J-mixing. The $^5D_0 \rightarrow {}^7F_4$ transition is also considered as an ED transition [1].

Under the CTB excitation at 279 nm, we observed several interesting emission features compared to the emission spectrum recorded under 395 nm excitation (Figure 5a): (a) an unusually intense 575 nm peak corresponding to $^5D_0 \rightarrow {}^7F_0$ transition, which otherwise is forbidden by both ED and MD transitions [44], (b) increased Stark splitting, (c) enhanced intensity of the $^5D_0 \rightarrow {}^7F_3$ peak, and (d) a significant change of the A_{21} value. The possible reasons for these observations will be further discussed in the following sections.

3.6. PL Lifetime Spectra and QY

Figure 6a,b show the results of the luminescence lifetime measurements of the BZOE-2 sample under the excitations at 279 and 395 nm with three different emission wavelengths of 575, 591, and 612 nm corresponding to $^5D_0 \rightarrow {}^7F_0$, $^5D_0 \rightarrow {}^7F_1$, and $^5D_0 \rightarrow {}^7F_2$ transitions, respectively. For the BZOE-2 sample, the luminescence lifetime curves recorded under the 279 nm excitation (Figure 6a) demonstrated a biexponential behavior with two slopes and they can be approximated using the following equation:

$$I = A_0 + A_1 \exp(-t/\tau_1) + A_2 \exp(-t/\tau_2) \quad (1)$$

where A_1 and A_2 are the derived preexponential factors, and τ_1 and τ_2 are the lifetime values of the fast and slow decay components, respectively. The luminescence lifetime curves recorded under the 395 nm excitation (Figure 6b) could be fitted with monoexponential decay.

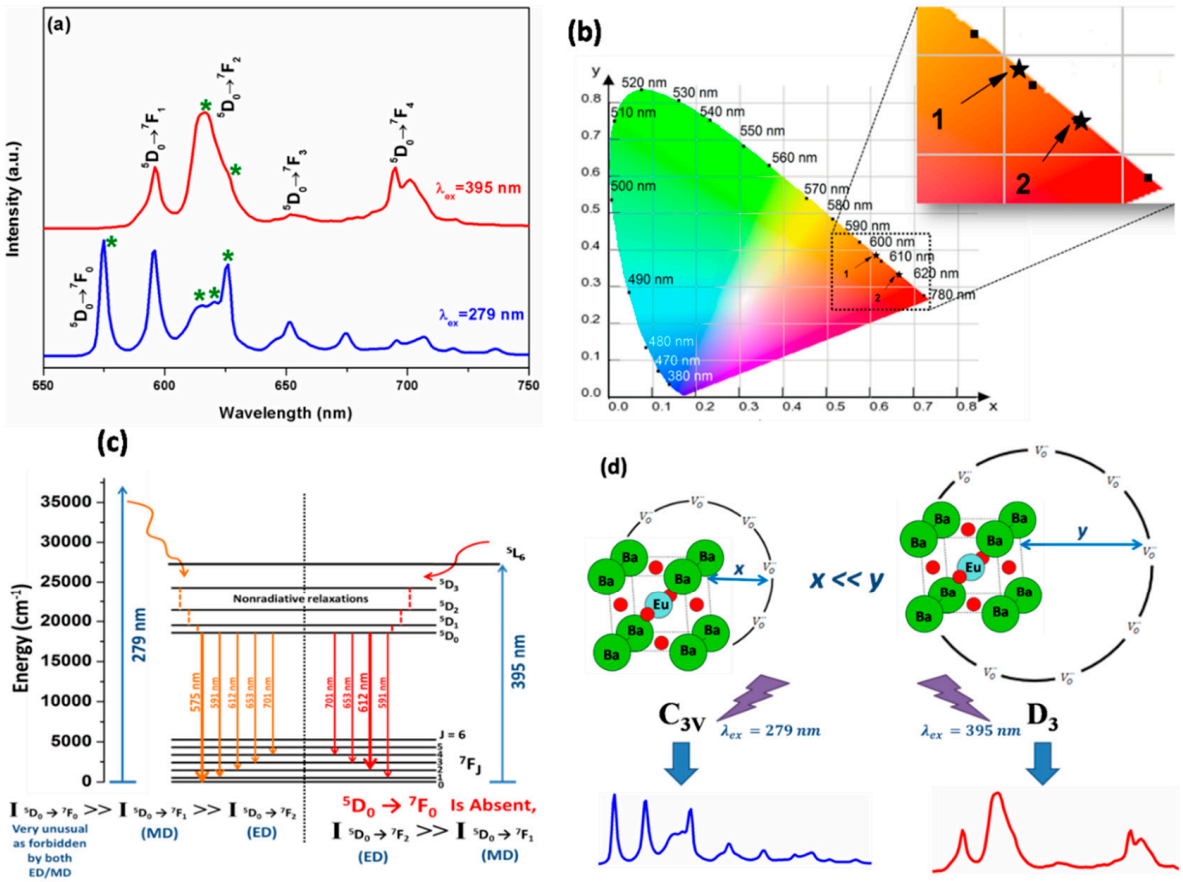

Figure 5. (**a**) Emission spectra of the BZOE-2 sample recorded at 77 K and (**b**) corresponding color coordinate diagram of the BZOE-2 sample under 279 and 395 nm excitations with * indicating the Stark components in (**a**) and arrows 1 and 2 pointing to the coordinates in (**b**), respectively. (**c**) Proposed photophysical processes happening under 279 and 395 nm excitations. (**d**) Schematic showing site selective excitations under 279 nm and 395 nm for the BZOE submicron crystals.

The population of Eu^{3+} ions with a particular lifetime is obtained by using the formula:

$$\% \text{ of species } n = (A_n * \tau_n)/(\Sigma_{n=1,2} A_n * \tau_n)] * 100 \quad (2)$$

Under λ_{ex} = 279 nm, there were two lifetime values for all three emissions: short lifetime T_s (~360–460 µs, 15%) and long lifetime T_l (~1.0–1.5 ms, 85%). On the other hand, under λ_{ex} = 395 nm, only one short lifetime value was obtained as T_s (~370–580 µs).

The decay profiles of all other BZOE samples are mentioned in Figure S6. Under λ_{ex} = 279 nm and λ_{em} = 625 nm, the average lifetime values of the BZOE samples with Eu^{3+} doping levels of 0.5, 1.0, 2.0, 5.0, and 10.0% were 789, 820, 950, 853, and 813 µs, respectively. The effect of Eu^{3+} concentration on the average lifetime value of the BZOE samples (Figure 6c) indicated that the average lifetime value increased up to a 2.0% Eu^{3+} doping level. Beyond that doping concentration, there was a reduction due to concentration quenching, which is consistent with the phenomenon observed from the PL excitation and emission spectra shown in Figure 4.

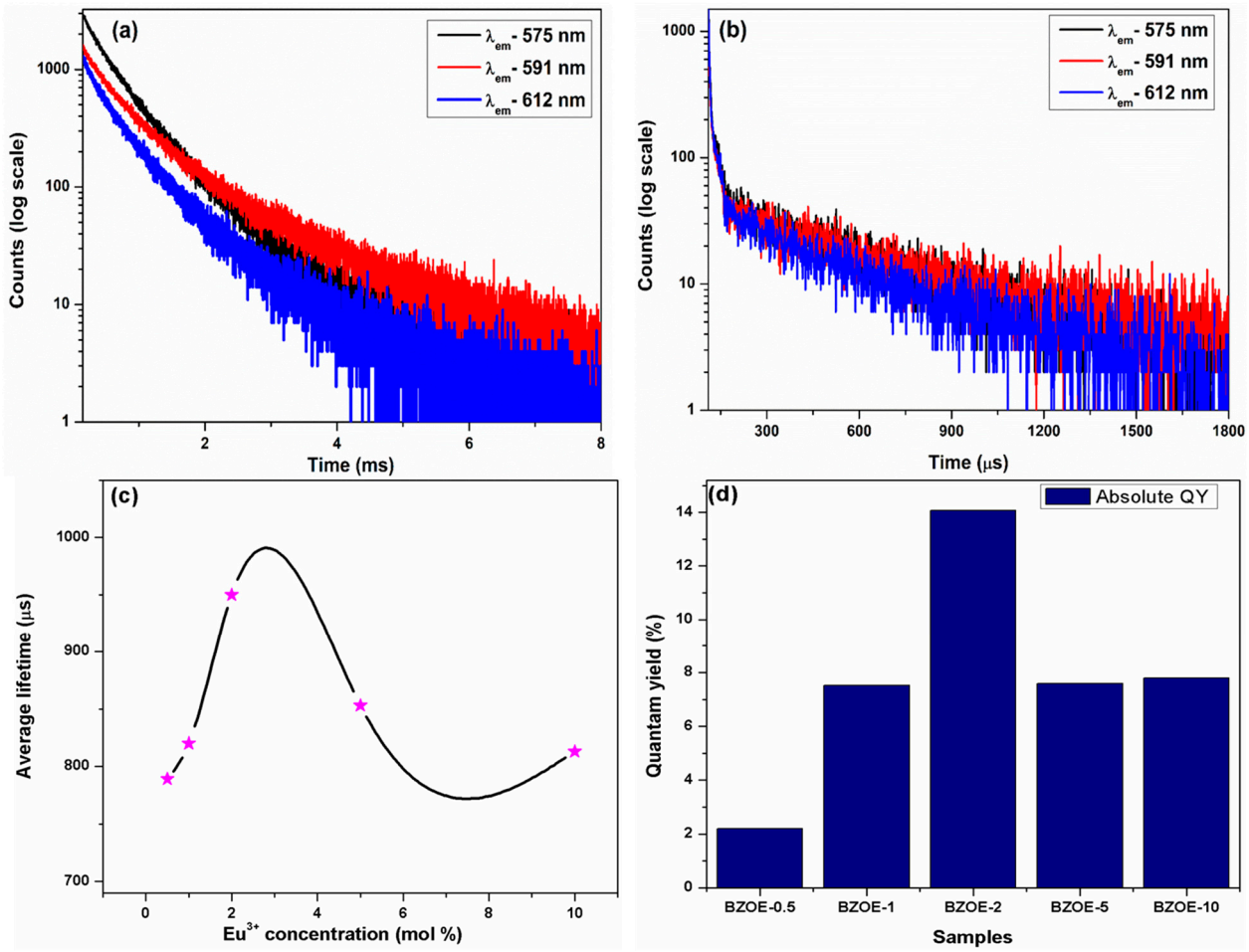

Figure 6. PL decay profiles of the BZOE-2 sample under excitation wavelengths of (**a**) 279 nm and (**b**) 395 nm at three different emission wavelengths of 575, 591, and 612 nm corresponding to $^5D_0 \rightarrow {}^7F_0$, $^5D_0 \rightarrow {}^7F_1$, and $^5D_0 \rightarrow {}^7F_2$ transitions of Eu^{3+} ions, respectively. (**c**) Effects of Eu^{3+} doping concentration of the BZOE samples on (**c**) average lifetime with * indicated the studied Eu^{3+} concentration (mol %) and (**d**) quantum yield (λ_{ex} = 279 nm and λ_{em} = 625 nm).

Quantum yield (QY) is an important parameter to evaluate the properties and application potentials of phosphors. We measured and calculated the QY of our BZOE samples using the following equation:

$$QY = \frac{\int F_S}{\int L_R + \int L_S} \quad (3)$$

where F_S represents the emission spectrum of a sample, L_R is the excitation spectrum from an empty integrating sphere (without any sample), and L_S means the excitation spectrum of a sample. The effect of the Eu^{3+} concentration on the QY value of the BZOE samples (Figure 6d) indicated that the QY value of the BZOE samples increased from 2.2% to 14.0% as the Eu^{3+} doping level increased from 0.5% to 2.0%. After higher dopant concentrations, the QY value reduced to ~7.6–7.9%. This is again attributed to concentration quenching arising from non-radiative energy transfer among Eu^{3+} ions at high doping concentrations.

Concentration quenching is one of the most dominant phenomena that takes place at high dopant concentrations. It is attributed to increasing resonant energy transfer between Eu^{3+} ions at a high dopant concentration, which results in decreasing radiative emissions. To better understand the mechanism of the concentration quenching phenomenon of our

BZOE samples, the critical distance (r_c) between Eu^{3+} dopant ions and quenching sites was calculated using the following equation:

$$r_c = 2\left(\frac{3V}{4\pi X_c N}\right)^{\frac{1}{3}} \quad (4)$$

where V, X_c, and N are the volume of the unit cell, the critical concentration of Eu^{3+} and the number of cations per unit cell, respectively. The values of these three variables for our BZOE samples are 73.6575 $Å^3$, 0.02, and 8, respectively. Hence, the calculated critical distance r_c value was 9.58 Å. Since the Eu^{3+}–Eu^{3+}critical distance is more than 5 Å, multipolar interactions are responsible for the concentration quenching of our BZOE crystals. Therefore, various PL studies indicated that there is a close correlation between the doping concentration with the excitation and emission intensity, luminescence lifetime, and the QY of the BZOE crystals.

3.7. J–O Analysis

To explain the observed luminescence performance, J–O parameters were determined to provide empirical relations between the local site symmetry of Eu^{3+} ions in the BZO lattice, the crystal field strength of the BZO host lattice, and the Eu–O bond covalency and polarizability in the BZOE samples.[45] Based on various mathematical formulations, we have derived the radiative/non-radiative transition rates and the internal quantum efficiency of the BZOE-2 sample [45–47]. Various important optical parameters were calculated for the BZOE samples under the excitations at 279 and 395 nm (Table 3). The BZOE-2 sample had a higher internal quantum efficiency (IQE) under the 279 nm excitation compared to 395 nm excitation. Its non-radiative transition (A_{NR}, 787.4 s^{-1}) and radiative transition (A_R, 212.77 s^{-1}) values under 279 nm were lower compared to those under 395 nm excitation (A_{NR} = 2331 s^{-1} and A_R = 369 s^{-1}). When changing λ_{ex} from 279 nm to 395 nm, the increase in the A_{NR} value was higher than that of the A_R value.

Table 3. Calculated J–O parameters and radiative properties of the BZOE-2 sample (A_R = radiative Rate, A_{NR} = nonradiative rate, Ω_n = the Judd−Ofelt parameter, and β_n = branching ratio).

BZOE-2	A_R (s^{-1})	A_{NR} (s^{-1})	η(%)	Ω_2 ($\times 10^{-20}$)	Ω_4 ($\times 10^{-20}$)	β_1(%)	β_2(%)	β_4(%)	Ω_2/Ω_4
λ_{ex} = 279 nm	212.77	787.4	21.3	1.04	0.917	23.5	42.4	18.6	1.13
λ_{ex} = 395 nm	369	2331	13.7	2.27	2.78	13.6	53.7	32.5	0.82

For the J–O parameters, Ω_2 (the short range parameter) gives information related to the covalent character, local symmetry, and structural distortion in the vicinity of Eu^{3+} ions, whereas Ω_4 intensity parameters (the long range parameter) provides bulk information such as the viscosity and rigidity of the host lattice [48]. Under the 279 nm excitation, the observed trend of the J–O parameters ($\Omega_4 < \Omega_2$) suggested that excited Eu^{3+} ions were mostly localized in a highly asymmetric and distorted environment. On the other hand, under the 395 nm excitation, the J–O parameter trend reversed with $\Omega_4 > \Omega_2$, which confirmed that a large fraction of excited Eu^{3+} ions occupies relatively less distorted and asymmetric sites. The value of the J–O ratio (Ω_2/Ω_4) of lower than one suggests a high asymmetry of the Eu^{3+} environment where its value higher than one suggests a low asymmetry. The fractional distribution of branching ratios suggests that, under the 279 and 395 nm excitations, photon parts emitted via MDT are 23.5% and 13.6%, whereas those emitted via HEDT are 42.4% and 53.7%, respectively.

3.8. Discussion

As marked by numbers one and two on the color coordinated diagram (Figure 5b), the intense peaks around 575 nm and 612 nm impart orange emissions under λ_{ex} = 279 nm and red emissions under λ_{ex} = 395 nm, respectively. It demonstrated that one can achieve

orange–red color tunability by selectively exciting the same material with dopant or host excitations. The different photophysical processes happening under these two excitations are schematically depicted in Figure 5d. The different spectral features of the BZOE samples observed under the 279 and 395 nm excitations suggest that the excited Eu^{3+} ions are relaxed through different channels to the ground states.

Some authors have proposed theoretical models for the observed $^5D_0 \rightarrow {}^7F_0$ transition, including the breakdown of the closure approximation in the Judd–Ofelt theory and third order perturbation theory [1,32,33]. The most obvious explanation assumes that this transition is due to J-mixing or to the mixing of low-lying charge-transfer states into the wave functions of the $4f^6$ configuration. Experimentally, the number of Stark components of the $^5D_0 \rightarrow {}^7F_0$ transition indicates the number of local sites of Eu^{3+} ions in host lattices. It is normally allowed when Eu^{3+} ions are situated at sites lacking inversion symmetry [1,49]. The presence of an unsplitted single band of the $^5D_0 \rightarrow {}^7F_0$ transition under λ_{ex} = 279 nm suggests that a large fraction of Eu^{3+} ions are located at the non-inversion symmetric sites in the BZOE submicron crystals. This hypothesis is further supported by the appearance of forbidden $^5D_0 \rightarrow {}^7F_3$ peaks with large Stark splitting [30,44]. On the other hand, under λ_{ex} = 395 nm, the observed phenomena, including the absence of $^5D_0 \rightarrow {}^7F_0$ transition, weak $^5D_0 \rightarrow {}^7F_3$ transition, and a low extent of Stark splitting of $^5D_0 \rightarrow {}^7F_1$ and $^5D_0 \rightarrow {}^7F_2$ transitions, suggest that a large fraction of Eu^{3+} ions at doping sites, which are less asymmetric or distorted, are selectively excited.

Based on the selection rules of point group symmetry, the $^5D_0 \rightarrow {}^7F_0$ transition appears when Eu^{3+} dopants are located at sites lacking an inversion center with 10 designated non-cubic point groups, including C_{6v}, C_6, C_{3v}, C_3, C_{4v}, C_4, C_{2v}, C_2, C_s, and C_1 [50]. The $^5D_0 \rightarrow {}^7F_0$ transition is not allowed in cubic groups with inversion symmetry such as T, T_d, and O or non-cubic point groups without inversion symmetry such as D_2, D_3, D_{3h}, C_{3h}, D_3, D_4, S_4, D_{2d}, D_{4d}, and D_6 [49].

The ideal BZO is a perfect cubic perovskite with O_h point group symmetry (space group: *Pm*-3*m*), which has 12-coordinated Ba^{2+} sites and 6-coordinated Zr^{4+} sites in cuboctahedra and octahedral geometries, respectively [51]. The observed emission spectra are in line with Eu^{3+} ions occupying the Zr^{4+} sites in the BZOE samples even with the following ionic radii values of Ba^{2+} (r_{ion} = 161 pm @ CN = 12), Zr^{4+} (r_{ion} = 72 pm @ CN = 6), and Eu^{3+} ions (r_{ion} = 95 pm @ CN = 6). Substituting Eu^{3+} ions at the Zr^{4+} sites distorts the symmetric ideal perovskite structure of BZO and invokes charge compensation by oxygen vacancies, which reduce the point group symmetry from O_h to further lower symmetry. This is consistent with our EXAFS analysis (Figure 3), especially at a low Eu^{3+} doping level before the low amount of Eu_2O_3 phase forms.

It has been reported that the emission of Eu^{3+} dopant in a cubic structure with the O_h point group should only have a single unsplitted $^5D_0 \rightarrow {}^7F_1$ transition peak [52]. By considering the most sensitive peaks for $^5D_0 \rightarrow {}^7F_0$ and $^5D_0 \rightarrow {}^7F_2$ transitions, there are 0 and 2 Stark components under λ_{ex} = 395 nm and 1 and 3 Stark components under λ_{ex} = 279 nm, respectively (Figure 5a). This observation suggested D_3 and C_{3V} point group symmetry around Eu^{3+} ions in our BZOE samples [52].

The Kroger–Vink notation for the substitution, wherein trivalent Eu^{3+} ions occupy tetravalent Zr^{4+} sites, is formulated below [53]:

$$2Eu^{\cdots} + Zr_{Zr}^{\times} \leftrightarrow Eu'_{Zr} + V_{\ddot{O}} \quad (5)$$

Defects such as $V_{\ddot{O}}$ and Eu'_{Zr} in the BZOE crystals provide additional pathways for non-radiative relaxation. They tend to quench PL by absorbing emitted photon energy from Eu^{3+} ion centers ($Eu_{Ba}^{\cdot}$) [47]. Hence, although Eu^{3+} ions occupy Zr^{4+} sites (Eu'_{Zr}), we assume that there are enough oxygen vacancies surrounding them with random distribution. There would be two scenarios: one with enough Eu'_{Zr} surrounded by oxygen vacancies in a close vicinity (x), designated as xEu'_{Zr}, and another with Eu'_{Zr} surrounded by oxygen vacancies at a much farther-off distance (y), designated as yEu'_{Zr}, such as y >> x. The point group symmetry of xEu'_{Zr}, as discussed above, is $C_{3v,}$ and that of yEu'_{Zr} is D_3. As schematically

shown in Figure 5d, upon the excitation with the Eu^{3+} *f-f* band at 395 nm, the prevalent excited species is yEu'_{Zr}, whereas upon excitation with the host CTB selectively, a large fraction excited species is xEu'_{Zr}.

4. Conclusions

In this work, BZOE submicron crystals with varied Eu^{3+} doping concentrations were synthesized using the molten salt method. XANES and EXAFS spectroscopies confirm that Eu is stabilized in a +3 oxidation state at Zr^{4+} s at a low doping concentration, while a separate Eu_2O_3 phase forms at the highest 10% doping level. Based on the PL measurement, it was established that europium is localized at Zr^{4+} sites in two different environments: one close to zirconium vacancies with C_{3v} symmetry and one far off from zirconium vacancies with D_3 symmetry. Interestingly, when excited at the charge transfer band of the BZO host at 279 nm, a large fraction of Eu^{3+} ions at non-symmetric C_{3v} sites were excited to give a highly intense $^5D_0 \rightarrow {}^7F_0$ transition, large spectral splitting, and intense MDT peaks compared to HEDT peaks. On the other hand, when excited at a dopant transition wavelength of 395 nm, a relatively large fraction of Eu^{3+} dopants, which are far off from zirconium vacancies with D_3 symmetry, were excited to give no $^5D_0 \rightarrow {}^7F_0$ transition, highly intense HEDT peaks compared to MDT peaks, and fewer Stark components. This excitation wavelength dependence induces emission light tunability of orange light at λ_{ex} = 279 nm and red light at λ_{ex} = 395 nm from the BZOE samples. This observation is further justified by the trend of the J–O parameters, especially with $\Omega_4 < \Omega_2$ at λ_{ex} = 279 nm and $\Omega_4 > \Omega_2$ at λ_{ex} = 395 nm. This work demonstrates the role of local dopant sites, defects, excitation wavelengths, and doping concentrations on optimizing the optical properties of lanthanide-doped perovskite phosphors for efficient optoelectronics and scintillator applications.

Supplementary Materials: The following are available online at https://www.mdpi.com/article/10.3390/nano12173028/s1, Experimental details. Figure S1. Size distribution plot for BZOE for different europium concentration derived using ImageJ software; Figure S2: Rietveld refinements for the BZOE samples; Figure S3: Ba L_3 edge fits for the three Eu-doped samples; Table S1: Fit parameters for Ba L_3 edge fits; Figure S4: Zr K edge fits for the three Eu-doped samples; Table S2: Fit parameters for Zr K edge fits; Figure S5: Eu L_3 edge fits for the three Eu-doped samples; Figure S6: PL decay profiles of the various BZOE sample under excitation wavelengths of 279 nm and emission wavelengths of 625 nm corresponding $^5D_0 \rightarrow {}^7F_2$ transitions of Eu^{3+} ions. References [34,54–57] are cited in the Supplementary Materials.

Author Contributions: Conceptualization, Y.M.; methodology, Y.M., S.K.G. and C.U.S.; validation, S.K.G., H.A. and C.U.S.; formal analysis, S.K.G. and C.U.S.; investigation, S.K.G. and C.U.S.; resources, Y.M.; data curation, S.K.G., H.A. and C.U.S.; writing—original draft preparation, S.K.G. and C.U.S.; writing—review and editing, Y.M.; visualization, S.K.G. and C.U.S.; supervision, Y.M.; project administration, Y.M.; funding acquisition, Y.M. All authors have read and agreed to the published version of the manuscript.

Funding: YM thanks the financial support by the IIT startup funds. SKG thanks the United States-India Education Foundation (USIEF, India) and the Institute of International Education (IIE, USA) for his Fulbright Nehru Postdoctoral Fellowship (Award #2268/FNPDR/2017). MRCAT operations are supported by the Department of Energy and the MRCAT member institutions. This research used resources of the Advanced Photon Source, a U.S. Department of Energy (DOE) Office of Science User Facility operated for the DOE Office of Science by Argonne National Laboratory under Contract No. DE-AC02-06CH11357.

Institutional Review Board Statement: Not applicable.

Informed Consent Statement: Not applicable.

Data Availability Statement: Data is contained within the article or supplementary materials.

Conflicts of Interest: The authors declare no conflict of interest.

References

1. Binnemans, K. Interpretation of europium(III) spectra. *Coord. Chem. Rev.* **2015**, *295*, 1–45. [CrossRef]
2. Gupta, S.K.; Rajeshwari, B.; Achary, S.N.; Patwe, S.J.; Tyagi, A.K.; Natarajan, V.; Kadam, R.M. Europium Luminescence as a Structural Probe: Structure-Dependent Changes in Eu^{3+}-Substituted $Th(C_2O_4)_2 \cdot xH_2O$ (x = 6, 2, and 0). *Eur. J. Inorg. Chem.* **2015**, *2015*, 4429–4436. [CrossRef]
3. Atuchin, V.; Aleksandrovsky, A.; Chimitova, O.; Gavrilova, T.; Krylov, A.; Molokeev, M.; Oreshonkov, A.; Bazarov, B.; Bazarova, J. Synthesis and spectroscopic properties of monoclinic α-$Eu_2(MoO_4)_3$. *J. Phys. Chem. C* **2014**, *118*, 15404–15411. [CrossRef]
4. Atuchin, V.; Subanakov, A.; Aleksandrovsky, A.; Bazarov, B.; Bazarova, J.; Gavrilova, T.; Krylov, A.; Molokeev, M.; Oreshonkov, A.; Stefanovich, S.Y. Structural and spectroscopic properties of new noncentrosymmetric self-activated borate $Rb_3EuB_6O_{12}$ with B_5O_{10} units. *Mater. Des.* **2018**, *140*, 488–494. [CrossRef]
5. Kitagawa, Y.; Ueda, J.; Fujii, K.; Yashima, M.; Funahashi, S.; Nakanishi, T.; Takeda, T.; Hirosaki, N.; Hongo, K.; Maezono, R.; et al. Site-Selective Eu^{3+} Luminescence in the Monoclinic Phase of $YSiO_2N$. *Chem. Mater.* **2021**, *33*, 8873–8885. [CrossRef]
6. Gupta, S.K.; Zuniga, J.P.; Ghosh, P.S.; Abdou, M.; Mao, Y. Correlating Structure and Luminescence Properties of Undoped and Eu^{3+}-Doped $La_2Hf_2O_7$ Nanoparticles Prepared with Different Coprecipitating pH Values through Experimental and Theoretical Studies. *Inorg. Chem.* **2018**, *57*, 11815–11830. [CrossRef]
7. Zhang, Y.; Xu, J.; Cui, Q.; Yang, B. Eu^{3+}-doped $Bi_4Si_3O_{12}$ red phosphor for solid state lighting: Microwave synthesis, characterization, photoluminescence properties and thermal quenching mechanisms. *Sci. Rep.* **2017**, *7*, 42464. [CrossRef]
8. Gupta, S.K.; Ghosh, P.S.; Yadav, A.K.; Pathak, N.; Arya, A.; Jha, S.N.; Bhattacharyya, D.; Kadam, R.M. Luminescence properties of $SrZrO_3/Tb^{3+}$ perovskite: Host-dopant energy-transfer dynamics and local structure of Tb^{3+}. *Inorg. Chem.* **2016**, *55*, 1728–1740. [CrossRef]
9. Kunkel, N.; Meijerink, A.; Springborg, M.; Kohlmann, H. Eu(ii) luminescence in the perovskite host lattices $KMgH_3$, $NaMgH_3$ and mixed crystals $LiBa_xSr_{1-x}H_3$. *J. Mater. Chem. C* **2014**, *2*, 4799–4804. [CrossRef]
10. Orvis, T.; Surendran, M.; Liu, Y.; Niu, S.; Muramoto, S.; Grutter, A.J.; Ravichandran, J. Electron Doping $BaZrO_3$ via Topochemical Reduction. *ACS Appl. Mater. Interfaces* **2019**, *11*, 21720–21726. [CrossRef] [PubMed]
11. Leonidov, I.I.; Tsidilkovski, V.I.; Tropin, E.S.; Vlasov, M.I.; Putilov, L.P. Acceptor doping, hydration and band-gap engineering of $BaZrO_3$. *Mater. Lett.* **2018**, *212*, 336–338. [CrossRef]
12. Gupta, S.K.; Pathak, N.; Kadam, R. An efficient gel-combustion synthesis of visible light emitting barium zirconate perovskite nanoceramics: Probing the photoluminescence of Sm^{3+} and Eu^{3+} doped $BaZrO_3$. *J. Lumin.* **2016**, *169*, 106–114. [CrossRef]
13. Charoonsuk, T.; Vittayakorn, N. Soft-mechanochemical synthesis of monodispersed $BaZrO_3$ sub-microspheres: Phase formation and growth mechanism. *Mater. Des.* **2017**, *118*, 44–52. [CrossRef]
14. Guo, L.; Zhong, C.; Wang, X.; Li, L. Synthesis and photoluminescence properties of Er^{3+} doped $BaZrO_3$ nanotube arrays. *J. Alloys Compd.* **2012**, *530*, 22–25. [CrossRef]
15. Vøllestad, E.; Strandbakke, R.; Tarach, M.; Catalán-Martínez, D.; Fontaine, M.-L.; Beeaff, D.; Clark, D.R.; Serra, J.M.; Norby, T. Mixed proton and electron conducting double perovskite anodes for stable and efficient tubular proton ceramic electrolysers. *Nat. Mater.* **2019**, *18*, 752–759. [CrossRef]
16. Ma, X.; Zhang, J.; Li, H.; Duan, B.; Guo, L.; Que, M.; Wang, Y. Violet blue long-lasting phosphorescence properties of Mg-doped $BaZrO_3$ and its ability to assist photocatalysis. *J. Alloys Compd.* **2013**, *580*, 564–569. [CrossRef]
17. Foo, G.S.; Polo-Garzon, F.; Fung, V.; Jiang, D.-E.; Overbury, S.H.; Wu, Z. Acid–Base Reactivity of Perovskite Catalysts Probed via Conversion of 2-Propanol over Titanates and Zirconates. *ACS Catal.* **2017**, *7*, 4423–4434. [CrossRef]
18. Ding, J.; Balachandran, J.; Sang, X.; Guo, W.; Veith, G.M.; Bridges, C.A.; Rouleau, C.M.; Poplawsky, J.D.; Bassiri-Gharb, N.; Ganesh, P. Influence of Nonstoichiometry on Proton Conductivity in Thin-Film Yttrium-Doped Barium Zirconate. *ACS Appl. Mater. Interfaces* **2018**, *10*, 4816–4823. [CrossRef]
19. Polfus, J.M.; Yildiz, B.; Tuller, H.L.; Bredesen, R. Adsorption of CO_2 and Facile Carbonate Formation on $BaZrO_3$ Surfaces. *J. Phys. Chem. C* **2018**, *122*, 307–314. [CrossRef]
20. Qi, S.; Wei, D.; Huang, Y.; Kim, S.I.; Yu, Y.M.; Seo, H.J. Microstructure of Eu^{3+}-Doped Perovskites-Type Niobate Ceramic $La_3Mg_2NbO_9$. *J. Am. Ceram. Soc.* **2014**, *97*, 501–506. [CrossRef]
21. Xie, J.; Shi, Y.; Zhang, F.; Li, G. $CaSnO_3$:Tb^{3+},Eu^{3+}: A distorted-perovskite structure phosphor with tunable photoluminescence properties. *J. Mater. Sci.* **2016**, *51*, 7471–7479. [CrossRef]
22. Pazik, R.; Tekoriute, R.; Håkansson, S.; Wiglusz, R.; Strek, W.; Seisenbaeva, G.A.; Gun'ko, Y.K.; Kessler, V.G. Precursor and solvent effects in the nonhydrolytic synthesis of complex oxide nanoparticles for bioimaging applications by the ether elimination (Bradley) reaction. *Chem. Eur. J.* **2009**, *15*, 6820–6826. [CrossRef] [PubMed]
23. Kunti, A.K.; Patra, N.; Harris, R.A.; Sharma, S.K.; Bhattacharyya, D.; Jha, S.N.; Swart, H.C. Local Structure and Spectroscopic Properties of Eu^{3+}-Doped $BaZrO_3$. *Inorg. Chem.* **2019**, *58*, 3073–3089. [CrossRef] [PubMed]
24. Kanie, K.; Seino, Y.; Matsubara, M.; Nakaya, M.; Muramatsu, A. Hydrothermal synthesis of $BaZrO_3$ fine particles controlled in size and shape and fluorescence behavior by europium doping. *New J. Chem.* **2014**, *38*, 3548–3555. [CrossRef]
25. Basu, S.; Patel, D.K.; Nuwad, J.; Sudarsan, V.; Jha, S.N.; Bhattacharyya, D.; Vatsa, R.K.; Kulshreshtha, S.K. Probing local environments in Eu^{3+} doped $SrSnO_3$ nano-rods by luminescence and Sr K-edge EXAFS techniques. *Chem. Phys. Lett.* **2013**, *561–562*, 82–86. [CrossRef]

26. Rabuffetti, F.A.; Culver, S.P.; Lee, J.S.; Brutchey, R.L. Local structural investigation of Eu^{3+}-doped $BaTiO_3$ nanocrystals. *Nanoscale* **2014**, *6*, 2909–2914. [CrossRef] [PubMed]
27. Canu, G.; Bottaro, G.; Buscaglia, M.T.; Costa, C.; Condurache, O.; Curecheriu, L.; Mitoseriu, L.; Buscaglia, V.; Armelao, L. Ferroelectric order driven Eu^{3+} photoluminescence in $BaZr_xTi_{1-x}O_3$ perovskite. *Sci. Reports* **2019**, *9*, 6441. [CrossRef]
28. Drąg-Jarząbek, A.; John, Ł.; Petrus, R.; Kosińska-Klähn, M.; Sobota, P. Alkaline Earth Metal Zirconate Perovskites $MZrO_3$ (M = Ba^{2+}, Sr^{2+}, Ca^{2+}) Derived from Molecular Precursors and Doped with Eu^{3+} Ions. *Chem. Eur. J.* **2016**, *22*, 4780–4788. [CrossRef]
29. Katyayan, S.; Agrawal, S. Effect of rare earth doping on optical and spectroscopic characteristics of $BaZrO_3$:Eu^{3+},Tb^{3+} perovskites. *Methods Appl. Fluoresc.* **2018**, *6*, 035002. [CrossRef]
30. Gupta, S.K.; Mohapatra, M.; Natarajan, V.; Godbole, S.V. Site-specific luminescence of Eu^{3+} in gel-combustion-derived strontium zirconate perovskite nanophosphors. *J. Mater. Sci.* **2012**, *47*, 3504–3515. [CrossRef]
31. Guo, Y.; Park, S.H.; Choi, B.C.; Jeong, J.H.; Kim, J.H. Dual-Mode Manipulating Multicenter Photoluminescence in a Single-Phased $Ba_9Lu_2Si_6O_{24}$:Bi^{3+},Eu^{3+} Phosphor to Realize White Light/Tunable Emissions. *Sci. Rep.* **2017**, *7*, 15884. [CrossRef]
32. Guzmán-Olguín, J.; Esquivel, R.L.; Jasso, G.T.; Guzmán-Mendoza, J.; Montalvo, T.R.; García-Hipólito, M.; Falcony, C. Luminescent behavior of Eu^{3+} doped $BaHfO_3$ perovskite ceramic under UV radiation. *Appl. Radiat. Isot.* **2019**, *153*, 108815. [CrossRef]
33. Gupta, S.K.; Reghukumar, C.; Kadam, R. Eu^{3+} local site analysis and emission characteristics of novel $Nd_2Zr_2O_7$:Eu phosphor: Insight into the effect of europium concentration on its photoluminescence properties. *RSC Adv.* **2016**, *6*, 53614–53624. [CrossRef]
34. Zhou, H.; Mao, Y.; Wong, S.S. Shape control and spectroscopy of crystalline $BaZrO_3$ perovskite particles. *J. Mater. Chem.* **2007**, *17*, 1707–1713. [CrossRef]
35. Charoonsuk, T.; Vittayakorn, W.; Vittayakorn, N.; Seeharaj, P.; Maensiri, S. Sonochemical synthesis of monodispersed perovskite barium zirconate ($BaZrO_3$) by using an ethanol–water mixed solvent. *Ceram. Int.* **2015**, *41*, S87–S94. [CrossRef]
36. Li, C.-C.; Chang, S.-J.; Lee, J.-T.; Liao, W.-S. Efficient hydroxylation of $BaTiO_3$ nanoparticles by using hydrogen peroxide. *Colloids Surf. A Physicochem. Eng. Asp.* **2010**, *361*, 143–149. [CrossRef]
37. Wirunchit, S.; Charoonsuk, T.; Vittayakorn, N. Facile sonochemical synthesis of near spherical barium zirconate titanate ($BaZr_{1-y}Ti_yO_3$; BZT); perovskite stability and formation mechanism. *RSC Adv.* **2015**, *5*, 38061–38074. [CrossRef]
38. Zeng, C.-H.; Zheng, K.; Lou, K.-L.; Meng, X.-T.; Yan, Z.-Q.; Ye, Z.-N.; Su, R.-R.; Zhong, S. Synthesis of porous europium oxide particles for photoelectrochemical water splitting. *Electrochim. Acta* **2015**, *165*, 396–401. [CrossRef]
39. Fassbender, R.U.; Lilge, T.S.; Cava, S.; Andrés, J.; da Silva, L.F.; Mastelaro, V.R.; Longo, E.; Moreira, M.L. Fingerprints of short-range and long-range structure in $BaZr_{1-x}Hf_xO_3$ solid solutions: An experimental and theoretical study. *Phys. Chem. Chem. Phys.* **2015**, *17*, 11341–11349. [CrossRef]
40. Giannici, F.; Longo, A.; Balerna, A.; Kreuer, K.-D.; Martorana, A. Proton Dynamics in In:$BaZrO_3$: Insights on the Atomic and Electronic Structure from X-ray Absorption Spectroscopy. *Chem. Mater.* **2009**, *21*, 2641–2649. [CrossRef]
41. Shi, P.; Xia, Z.; Molokeev, M.S.; Atuchin, V.V. Crystal chemistry and luminescence properties of red-emitting $CsGd_{1-x}Eux(MoO_4)_2$ solid-solution phosphors. *Dalton Trans.* **2014**, *43*, 9669–9676. [CrossRef] [PubMed]
42. Denisenko, Y.G.; Molokeev, M.S.; Oreshonkov, A.S.; Krylov, A.S.; Aleksandrovsky, A.S.; Azarapin, N.O.; Andreev, O.V.; Razumkova, I.A.; Atuchin, V.V. Crystal structure, vibrational, spectroscopic and thermochemical properties of double sulfate crystalline hydrate $[CsEu(H_2O)_3(SO_4)_2]\cdot H_2O$ and its thermal dehydration product $CsEu(SO_4)_2$. *Crystals* **2021**, *11*, 1027. [CrossRef]
43. Gupta, S.K.; Ghosh, P.S.; Yadav, A.K.; Jha, S.N.; Bhattacharyya, D.; Kadam, R.M. Origin of Blue-Green Emission in α-$Zn_2P_2O_7$ and Local Structure of Ln^{3+} Ion in α-$Zn_2P_2O_7$:Ln^{3+} (Ln = Sm, Eu): Time-Resolved Photoluminescence, EXAFS, and DFT Measurements. *Inorg. Chem.* **2017**, *56*, 167–178. [CrossRef] [PubMed]
44. Gupta, S.K.; Mohapatra, M.; Kaity, S.; Natarajan, V.; Godbole, S.V. Structure and site selective luminescence of sol–gel derived Eu:Sr_2SiO_4. *J. Lumin.* **2012**, *132*, 1329–1338. [CrossRef]
45. Jain, N.; Paroha, R.; Singh, R.K.; Mishra, S.K.; Chaurasiya, S.K.; Singh, R.A.; Singh, J. Synthesis and Rational design of Europium and Lithium Doped Sodium Zinc Molybdate with Red Emission for Optical Imaging. *Sci. Rep.* **2019**, *9*, 2472. [CrossRef]
46. Gupta, S.K.; Mohapatra, M.; Godbole, S.V.; Natarajan, V. On the unusual photoluminescence of Eu^{3+} in α-$Zn_2P_2O_7$: A time resolved emission spectrometric and Judd–Ofelt study. *RSC Adv.* **2013**, *3*, 20046–20053. [CrossRef]
47. Gupta, S.K.; Sudarshan, K.; Ghosh, P.S.; Srivastava, A.P.; Bevara, S.; Pujari, P.K.; Kadam, R.M. Role of various defects in the photoluminescence characteristics of nanocrystalline $Nd_2Zr_2O_7$: An investigation through spectroscopic and DFT calculations. *J. Mater. Chem. C* **2016**, *4*, 4988–5000. [CrossRef]
48. Vats, B.G.; Gupta, S.K.; Keskar, M.; Phatak, R.; Mukherjee, S.; Kannan, S. The effect of vanadium substitution on photoluminescent properties of $KSrLa(PO_4)_x(VO_4)_{2-x}$:$Eu^{3+}$ phosphors, a new variant of phosphovanadates. *New J. Chem.* **2016**, *40*, 1799–1806. [CrossRef]
49. Tanner, P.A. Some misconceptions concerning the electronic spectra of tri-positive europium and cerium. *Chem. Soc. Rev.* **2013**, *42*, 5090–5101. [CrossRef]
50. Chen, X.; Liu, G. The standard and anomalous crystal-field spectra of Eu^{3+}. *J. Solid State Chem.* **2005**, *178*, 419–428. [CrossRef]
51. Manju, P.; Ajith, M.R.; Jaiswal-Nagar, D. Synthesis and characterization of $BaZrO_3$ nanoparticles by citrate-nitrate sol-gel auto-combustion technique: Systematic study for the formation of dense $BaZrO_3$ ceramics. *J. Eur. Ceram. Soc.* **2019**, *39*, 3756–3767. [CrossRef]

52. Ju, Q.; Liu, Y.; Li, R.; Liu, L.; Luo, W.; Chen, X. Optical Spectroscopy of Eu^{3+}-Doped BaFCl Nanocrystals. *J. Phys. Chem. C* **2009**, *113*, 2309–2315. [CrossRef]
53. Gupta, S.K.; Sudarshan, K.; Yadav, A.K.; Gupta, R.; Bhattacharyya, D.; Jha, S.N.; Kadam, R.M. Deciphering the Role of Charge Compensator in Optical Properties of $SrWO_4$:Eu^{3+}:A (A = Li^+, Na^+, K^+): Spectroscopic Insight Using Photoluminescence, Positron Annihilation, and X-ray Absorption. *Inorg. Chem.* **2018**, *57*, 821–832. [CrossRef]
54. Toby, B.H.; Von Dreele, R.B. GSAS-II: The genesis of a modern open-source all purpose crystallography software package. *J. Appl. Crystallogr.* **2013**, *46*, 544–549. [CrossRef]
55. Kropf, A.; Katsoudas, J.; Chattopadhyay, S.; Shibata, T.; Lang, E.; Zyryanov, V.; Ravel, B.; McIvor, K.; Kemner, K.; Scheckel, K. The new MRCAT (Sector 10) bending magnet beamline at the advanced photon source. *AIP Conf. Proc.* **2010**, *1234*, 299–302.
56. Newville, M. IFEFFIT: Interactive XAFS analysis and FEFF fitting. *J. Synchrotron Radiat.* **2001**, *8*, 322–324. [CrossRef]
57. Ravel, B.; Newville, M. ATHENA, ARTEMIS, HEPHAESTUS: Data analysis for X-ray absorption spectroscopy using IFEFFIT. *J. Synchrotron Radiat.* **2005**, *12*, 537–541. [CrossRef]